

# INCREASING THE DIMENSIONAL STABILITY OF $\text{CaO-FeO}_x\text{-Al}_2\text{O}_3\text{-SiO}_2$ ALKALI-ACTIVATED MATERIALS: ON THE SWELLING POTENTIAL OF CALCIUM OXIDE-RICH ADMIXTURES

Guilherme Ascensão<sup>1,\*</sup>, Maurizio Marchi<sup>1</sup>, Monica Segata<sup>1</sup>, Flora Faleschini<sup>2</sup> and Yiannis Pontikes<sup>3</sup>

<sup>1</sup> Italcementi SpA, via Stezzano 87, 24126 Bergamo, Italy

<sup>2</sup> University of Padova - Department of Civil, Environmental and Architectural Engineering, via Francesco Marzolo 9, 35131 Padova, Italy

<sup>3</sup> KU Leuven, Department of Materials Engineering, Kasteelpark Arenberg 44, 3000 Leuven, Belgium

## Article Info:

Received:  
1 July 2019  
Revised:  
14 October 2019  
Accepted:  
28 October 2019  
Available online:  
23 December 2019

## Keywords:

Alkali-activated materials  
Calcium oxide  
Construction materials  
Shrinkage control  
Upcycling

## ABSTRACT

Advanced thermochemical conversion processes are emerging technologies for materials' recovery and energetic conversion of wastes. During these processes, a (semi-)vitreous material is also produced, and as these technologies get closer to maturity and full-scale implementation, significant volumes of these secondary outputs are expected to be generated. The production of building materials through the alkali activation of such residues is often identified as a possible large-scale valorization route, but the high susceptibility of alkaliactivated materials (AAM) to shrinkage limits their attractiveness to the construction sector. Aiming to mitigate such a phenomenon, an experimental study was conducted investigating the effect of calcium oxide-rich admixtures on the dimensional stability of  $\text{CaO-FeO}_x\text{-Al}_2\text{O}_3\text{-SiO}_2$  AAMs. This work describes the impacts of such admixtures on autogenous and drying shrinkage, porosity, microstructure, and mineralogy on AAMs. Drying shrinkage was identified as the governing mechanism affecting AAM volumetric stability, whereas autogenous shrinkage was less significant. The reference pastes presented the highest drying shrinkage, while increasing the dosage of shrinkage reducing agent (SRA) was found to reduce drying shrinkage up to 63%. The reduction of drying shrinkage was proportional to SRA content; however, elevated dosages of such admixture were found to be detrimental for AAM microstructure. On the other hand, small dosages of calcium oxide-rich admixtures did not induce significant changes in the samples' mineralogical evolution but promoted the formation of denser and less fractured microstructures. The results presented here show that calcium oxide-rich admixtures can be used to increase AAM's volumetric stability and an optimal dosage is prescribed.

## 1. INTRODUCTION

Alkali-activated materials (AAMs) are emerging as potential alternatives to cementitious materials, due to a less energy-intensive production process with lower environmental burdens associated. Alkali activation can be described as the reaction of a solid aluminosilicate material with an alkaline medium - which is usually a concentrated aqueous solution of alkali hydroxide, silicates, carbonates or sulfates - to produce a hardened binder (Provis, 2014). Unlike cement manufacturing, alkali-activation does not involve high-temperature processes, being AAMs manufactured at room or slightly elevated temperatures (<100°C). The use of industrial by-products and residues in AAMs design aims to further reduce

their environmental footprint and production cost making them very interesting in the context of circular economy and increasing their competitiveness relative to ordinary Portland cement (OPC)-based systems. The research in this field has been mostly dedicated to metallurgical slags (Onisei et al., 2015; Komnitsas et al., 2019) but a wide group of yet unexplored waste streams can be used as AAMs precursors.

As gasification technologies of refuse-derived fuel (RDF) obtained via ELFM will reach maturity and are implemented worldwide, significant volumes of  $\text{CaO-FeO}_x\text{-Al}_2\text{O}_3\text{-SiO}_2$ -rich vitreous residues are expected to be generated in those thermal conversion processes. Currently, the use of such residues is limited to low-value applica-



tions (e.g. road paving) but alkali-activation technology can represent a promising large-scale and fruitful valorization route.

Apart from allowing to reintegrate significant volumes of residues into the materials cycle, AAMs can also present several technical advantageous features, such as superior compressive strength, fire resistance and chemical attack resistance (Cartwright et al., 2014). However, the acceptance and large-scale implementation of AAMs will greatly depend on their long-term performance in which volumetric stability is a key factor. In fact, high susceptibility to shrinkage of AAMs is frequently reported (Cartwright et al., 2014; Lee et al., 2014), which presents a major compromising factor to the widespread adoption of the alkali activation technology. During the alkali hydrolysis that initially disrupts the precursor's glassy structure, a significant amount of water is consumed. As dissolution continues and the concentration of dissolved species in the medium increases, oligomers start to be formed, which later further crosslinks to create polymers. The recombination and reorganization of these polymers result in a significant volume contraction and release the water consumed during dissolution (Duxson et al., 2007). This water remains in the pore structure of the binder without being chemically bonded (Pacheco-Torgal et al., 2012). The existence of significant amounts of free-water in IP systems later results in severe shrinkage, leading to the appearance of multiple micro to macro-cracks in the binder matrix.

In isothermal conditions, different shrinkage mechanism contributes to the IPs volumetric instability. Autogenous shrinkage offsets once the material initiate to consolidate and is driven by self-desiccation (Neto et al., 2008). Self-desiccation is generated in the pores as the pore solution continues to react with the pore surface to form additional binding phases. The saturation of the pores reduces and capillary pore tensions are generated (Jensen et al., 2001). Additional shrinkage results from evaporation processes when the materials are exposed to an open environment (drying shrinkage).

Methods to mitigate shrinkage have been extensively developed for OPC-based systems, however much fewer successful investigations have been reported in field alkali-activated systems, particularly when  $(\text{FeO}_x)\text{-CaO}$ -rich slags are used as precursors. In the cement industry, the swelling potential of oxide-based admixtures has been successfully used for decades to increase volumetric stability and counteract shrinkage effects (Ono et al., 1971; Chanvillard et al., 2007; Corinaldesi et al. 2015; Yang et al. 2019). Hydroxide formation from quicklime hydration has been broadly reported (Chen et al., 2012) but cement and AAMs' chemistry are entirely distinct, and the use of calcium compounds to compensate for shrinkage may affect the polymerization process and products formed (Guo et al., 2015). Van Deventer et al. (2007) investigated the effect of  $\text{Ca}^{2+}$  during the alkali activation of fly-ash and suggested that such cationic species rapidly dissolve and precipitate, providing a large number of extra potential nucleation sites. Kellermeier et al. (2010) investigated the progress of calcium carbonates in inorganic silica-rich environments and proposed that growing amorphous calcium carbonate parti-

cles can promote the spontaneous polymerization of silica.

These accelerating effects will compete with the removal of the  $\text{OH}^-$  ions from the solution, which has the net effect of lowering its pH. A decrease in solution pH will in turn affect further dissolution and precipitation processes, thus reducing supersaturation, which is the primary driving force for polymerization (Van Deventer et al., 2007). Additionally, the stability of calcium-containing precipitates also depends upon the medium composition and pH (Van Deventer et al., 2007), which render it difficult to define a general kinetic reaction model and to predict the effects of calcium-rich admixtures in specific mix designs. Nonetheless, Salman et al. (2015) observed very early exothermic peaks during the alkali activation of Ca-rich slags, from which the authors concluded that they must be related to the enhancement of reaction kinetics due to the hydrolysis of Si-O-Ca and Ca-O-Ca linkages.

However, the scarce literature on the effects of  $\text{Ca}^{2+}$  during alkali activation is focused on systems with low-iron content (Yuan et al., 2014; Velandia et al., 2016), whereas appreciable levels of iron will increase the complexity of the mechanisms involved. Daux et al. (1997) studied the dissolution of basaltic glasses and observed that Fe species are dissolved and precipitated faster than Si and Al. Van Deventer et al. (2007) reported that reactive Fe species will most likely behave similarly to  $\text{Ca}^{2+}$ , precipitating as hydroxide or oxy-hydroxide and decreasing the pH of the solution. Gomes et al. (2010) used  $^{57}\text{Fe}$  Mössbauer spectroscopy to determine the fate of iron during alkali activation and found that a small portion of  $\text{Al}^{3+}$  could be replaced by  $\text{Fe}^{3+}$  in octahedral sites. Nonetheless, Simon et al. (2018) demonstrated that AAMs produced from Fe-rich slags are structurally different from "Fe-enriched" aluminosilicate geopolymers, in more than just Fe-Al substitution in tetrahedrally-coordinated sites. In recent work, Peys et al. (2019) used in situ X-ray total scattering and subsequent pair distribution function (PDF) analysis to describe the formation mechanism of Fe-rich alkali-activated materials. They found that the atomic rearrangements undergone by Fe-silicate species are heavily dependent on the alkali cation provided by the activating solution. In the case of sodium, the atomic correlations of the parent precursors are maintained in the intermediate products, while potassium solutions induce an increase in the coordination number of Fe species. Moreover, it was reported that  $\text{Fe}^{2+}$  and  $\text{Fe}^{3+}$  oxidation states coexist in the binder phase under different forms. The  $\text{Fe}^{2+}$  state was observed to be present as trioctahedral layers, while the participation of  $\text{Fe}^{3+}$  in the polymerized silicate network seemed most likely. In addition, PDF analysis of matured specimens has shown significant modifications, suggesting the long-term oxidization of the  $\text{Fe}^{2+}$  species present in the trioctahedral layers.

From the above, it seems evident that some questions remain unanswered to enable a full understanding of the structural role of iron during alkali activation and, to a larger extent, to describe the effects of calcium "enrichment" in Fe-rich systems.

Hence, in the present study,  $\text{CaO-FeO}_x\text{-Al}_2\text{O}_3\text{-SiO}_2$  alkali-activated materials were produced and the impact of cal-

cium-rich admixtures on its autogenous and dry shrinkage, mineralogy, microstructure, and porosity was assessed. Combined with previous analyses on setting time and mechanical features (Ascensão et al., 2019b), a holistic overview was possible and an optimal admixture dosage is prescribed.

## 2. EXPERIMENTAL

### 2.1 Methods

X-ray fluorescence (Bruker AXS S8 Tiger spectrometer) was used to determine the bulk chemical composition of the materials used in this work; its surface area was determined via nitrogen adsorption/desorption methods, according to ISO 9277:2010.

All pastes and monolithic samples analyzed during this work were produced following the procedure described by Ascensão et al. (2017), in which two extra minutes were added to mix the shrinkage control agent. The samples were produced by pouring the pastes into metallic molds and curing them for 24 h in controlled conditions ( $20 \pm 0.5^\circ\text{C}$  and  $95 \pm 1\%$  relative humidity). Afterward, the samples were demolded and kept at room conditions ( $20^\circ\text{C}$  and 65 % relative humidity).

In order to investigate the dynamics of autogenous shrinkage, a laser measurement system was used (as shown in Figure 1). The set-up consisted of two laser units horizontally aligned and directed to lightweight reflectors placed on top of the pastes. A polypropylene foil was used to isolate the pastes from direct contact with the metallic mold and to minimize water evaporation. The distance between the lasers and the reflectors was recorded continuously for ten days and the sum of the relative displacements was converted into linear deformation.

To evaluate the impact of Ca-rich compounds on drying shrinkage, two types of samples were produced. For preliminary measurements, six samples ( $2 \times 2 \times 16 \text{ cm}^3$ ) were produced for each formulation, having a metallic spindle (type II) attached in each extremity. On selected formulations, two samples ( $4 \times 4 \times 16 \text{ cm}^3$ ) were produced with a metallic spindle (type I), according to EN 12617-4:2002. The length variation of samples was monitored using a dial

gauge with a sensitivity of 0.001 mm for up to 56 days after casting. Weight variation (with a precision of 0.01 g) was recorded during the same period.

The mineralogical composition of hardened samples was assessed by X-ray diffraction (XRD), conducted on a conventional Bragg-Brentano Bruker D8 Advance diffractometer, equipped with Lynxeye detector (Cu K $\alpha$  radiation  $\lambda = 1.54059 \text{ \AA}$ , divergence slit  $0.5^\circ$ , Soller slit set  $2.5^\circ + 2.5^\circ$ ,  $5-70^\circ 2\theta$ , step/size  $0.02^\circ$  and t/step 0.04s.), and phase identification using EVA software. All samples were collected from mechanical testing, then ground, sieved and low vacuum dried ( $40^\circ\text{C}$ ) for 3 h prior to testing. The mineralogical evolution of the samples was monitored on the 1st, 3rd, 7th and 28th days. Scanning electron microscopy (SEM - EVO<sup>®</sup> MA 15) equipped with energy dispersive X-ray spectrometry (EDS, AZtecEnergy) was used to evaluate the differences in morphology and microstructure of the produced samples after 28 days of curing. All backscattered electron images (BSE) were acquired using a 20 kV acceleration voltage and a work distance of 10.0 mm.

The pore size distribution of the samples was investigated by mercury intrusion porosimetry (MIP). Fractured samples from mechanical tests at 28 days of curing were collected and dried in a vacuum chamber for 5 hours ( $45^\circ\text{C}$ ) prior to testing. A mercury surface tension of 0.48 N/m and a contact angle of  $141.0^\circ$  were set for the MIP measurements.

### 2.2 Materials

A synthetic CaO-FeO<sub>x</sub>-Al<sub>2</sub>O<sub>3</sub>-SiO<sub>2</sub> rich vitreous material (referred to as plasmastone; hereafter PS) was used as the main precursor. Its detailed production process is described in Machiels et al. (2017). PS was dried, homogenized and milled, and it is composed of SiO<sub>2</sub> 35.1, CaO 22.9, FeO<sub>x</sub> 22.8, Al<sub>2</sub>O<sub>3</sub> 16.1, MgO 1.4, K<sub>2</sub>O 0.6, TiO<sub>2</sub> 0.6, Na<sub>2</sub>O 0.3, Mn<sub>2</sub>O<sub>3</sub> 0.1, SO<sub>3</sub> 0.1 and 1.9 wt% loss on ignition (LOI). Its BET surface area after milling was determined to be 1120 m<sup>2</sup>/kg and its particle size distribution is given in previous studies (Ascensão et al., 2019a).

Densified silica fume (hereafter, SF) was purchased from ELKEM<sup>®</sup> (Microsilica Grade 940) and used as an admixture to provide a secondary source of SiO<sub>2</sub>. The specific surface area (BET; 22210 m<sup>2</sup>/kg) and composition (XRF)

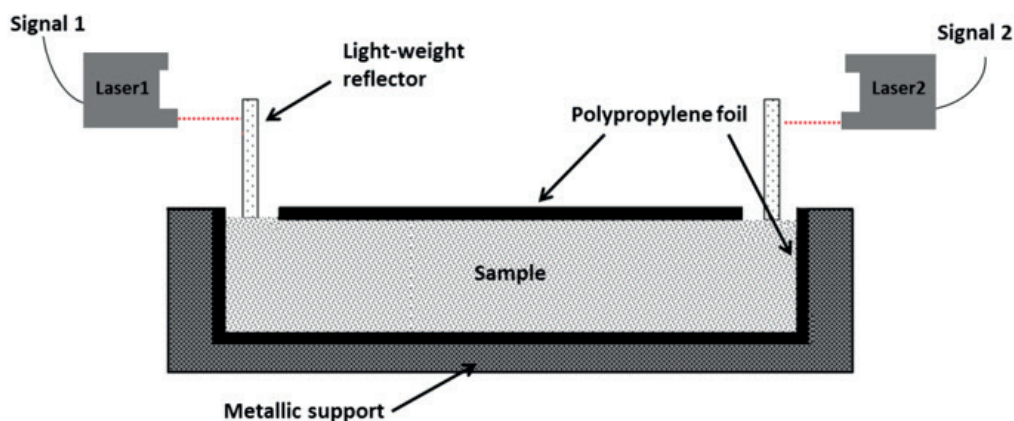


FIGURE 1: Schematic representation of autogenous shrinkage measurement apparatus.

of the SF were determined by laboratory experimentation. The SiO<sub>2</sub> content of the SF was 95.0 wt%, and minor elements present, such as CaO, Fe<sub>2</sub>O<sub>3</sub>, and Al<sub>2</sub>O<sub>3</sub>, were considered negligible (<0.5 wt%). A commercially available calcium-oxide rich material (Expandex C-NEW, Sika, Italy) was used as a shrinkage reducing agent (SRA). The SRA particle size was found to range between 0.1–67 μm, with d10, d50 and, d90 of 0.6, 4.3 and 27 μm, respectively. SRA was determined to be mainly composed of CaO 73.0, SiO<sub>2</sub> 3.6 and MgO 1.5 and minor contents of Fe<sub>2</sub>O<sub>3</sub>, Al<sub>2</sub>O<sub>3</sub>, K<sub>2</sub>O, TiO<sub>2</sub>, Na<sub>2</sub>O, Mn<sub>2</sub>O<sub>3</sub>, SO<sub>3</sub>, SrO, P<sub>2</sub>O<sub>5</sub> (all less than 1.0 wt%), with 21.0 wt% loss on ignition (LOI). X-ray diffraction patterns showed that PS and SF patterns exhibited a pronounced hump between 20-40° and 15-30° 2θ respectively, confirming their predominantly amorphous nature (Figure 2a). In the SF's XRD pattern only one crystalline peak was detected and identified as moissanite (SiC; PDF 02-1464). As can be seen in Figure 2b, the main minerals detected on the SRA pattern were calcite (CaCO<sub>3</sub>; PDF 00-005-0586), lime (CaO; PDF 00-037-1497) and portlandite (Ca(OH)<sub>2</sub>; PDF 00-004-0733).

Potassium hydroxide (14 M) and potassium silicate solutions (23.8 wt% SiO<sub>2</sub>, 9.5 wt% K<sub>2</sub>O and 66.7 wt% H<sub>2</sub>O) were prepared by dissolving potassium hydroxide beads (reagent grade, 85%, Carlo Erba, Italy) and anhydrous potassium silicate (-48 mesh; 2.5 SiO<sub>2</sub>:K<sub>2</sub>O wt%, Alfa Aesar, Germany) in demineralized water. The solutions were prepared in advance to allow them to cool down prior to the preparation of the pastes. The detailed description of the prepared pastes can be seen in Table 1. It should be noted that the analyzed pastes differ only by the amount of SRA, whereas the other mix components were kept constant.

### 3. RESULTS AND DISCUSSION

#### 3.1 AAM shrinkage characteristics

##### 3.1.1 Autogenous shrinkage

As briefly stated, alkali-activated materials are known to be several times more prone to shrinkage than OPC-based systems (Thomas et al., 2017). The swelling potential of calcium-rich admixtures can be used to compensate for this, thus enhancing AAM's long-term performance. In open conditions, autogenous and drying shrinkage occurs simultaneously, though the mechanisms involved are rather different. Autogenous shrinkage can be defined as a physico-chemical phenomenon that results from chemo-mechanical and hygro-mechanical interactions (Mounanga et al., 2011). The former is due to the difference between the absolute density of the reaction products and the starting materials (also known as chemical shrinkage), while the latter results from tensile stresses generated during the emptying of the pores as hydration reactions progress (also known as self-desiccation). In AAM synthesis, a high solid content is often used to achieve good mechanical performances and enhanced durability. Imposing such synthesis conditions, however, leads to the refinement of the pore structures, which inevitably enlarges capillary stress in partially filled pores, and so contributes to high autogenous shrinkage (Lee et al., 2014). Moreover, the high viscosity of silicate solutions, like the ones used in this work, considerably increases the viscosity of the activating solution, contributing to a further rise in surface tension in partially filled pores (Sakulich et al., 2013).

Figure 3 shows length variation due to autogenous shrinkage of the analyzed pastes as a function of SRA

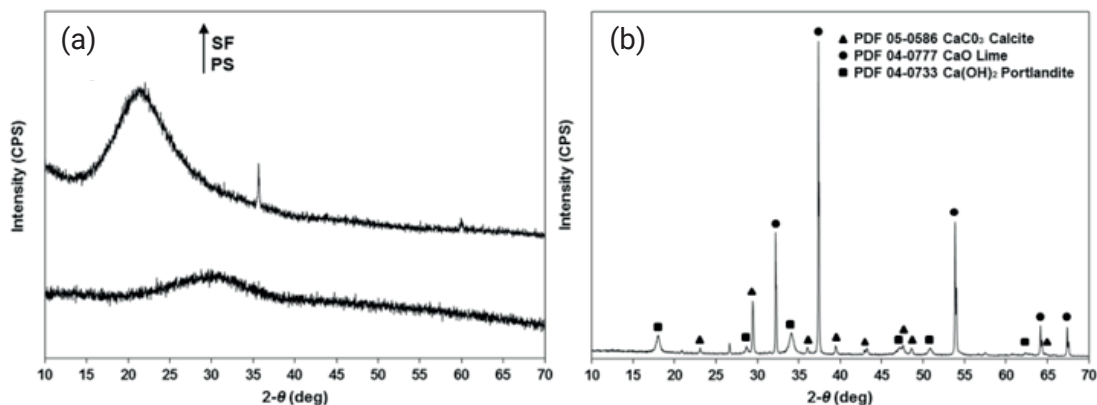
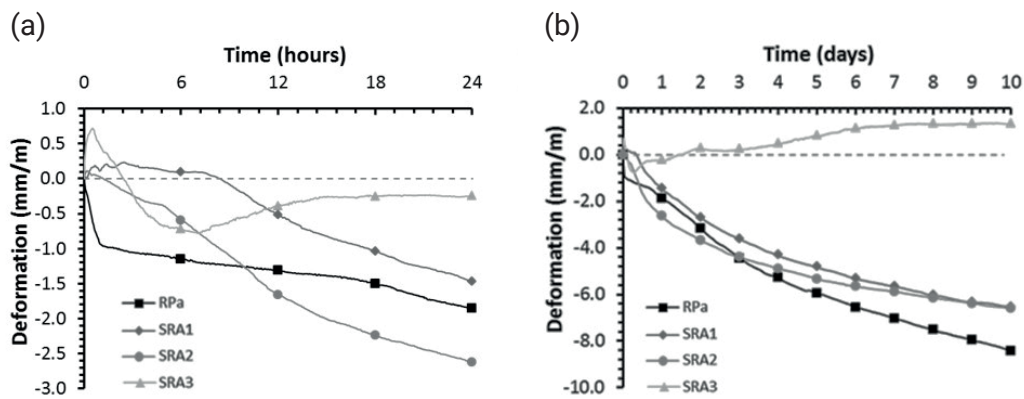


FIGURE 2: X-ray diffraction patterns of a) AAM raw materials, plasmastone and silica fume and b) shrinkage reducing agent.

TABLE 1: Classification of the landfilled material by categories.

Code	Mixture portion (wt%)					solid/liquid wt ratio	Admixtures (wt solid %)
	PS	SF	k-silicate (aq.)	KOH (aq.)	H <sub>2</sub> O		
RPa							0.0
SRA1	72.1	4.1	6.2	5.3	12.3	3.2	1.0
SRA2							2.0
SRA3							3.0



**FIGURE 3:** Autogenous shrinkage as a function of shrinkage reducing agent content: a) initial 24 hours and b) evolution until the tenth day of curing.

content and time. It can be seen that the reference paste presented high linear deformation during the testing period. In the initial stage of the reaction, considered to be the timeframe from mixing until the initial setting time ( $\approx 42$  minutes) (Ascensão et al., 2019b), capillary stresses can be negligible, and autogenous shrinkage is mainly attributed to chemical contraction. Thus, it is interesting to notice that shortly after that period, the autogenous shrinkage progression rate drastically reduces in the reference paste, which may indicate the point at which chemical shrinkage ceases and self-desiccation begins to dominate.

The addition of calcium-rich admixtures was expected to urge the formation of calcium hydrates species and/or increase the polymeric gel formation (Van Deventer et al., 2007; Guo et al., 2015) or promote the spontaneous Si-polymerization (Kellermeier et al., 2010), which could potentially affect both chemical and self-desiccation processes. Figure 3b shows that the addition of calcium oxide reduced autogenous shrinkage during the test period. In fact, samples with 1.0 and 2.0 wt% SRA underwent approximately 20.0% less length variation than the reference paste, while with higher SRA dosages a slight expansion occurred.

As calcium oxide was introduced, its finer fraction immediately hydrated and induced an initial expansion, as can be seen in Figure 3a. Depending on the SRA content, such expansion is able to partially mitigate or overcome early age autogenous shrinkage. The reasons for the distinct behavior of SRA1 and SRA2 at very early ages are not clear. However, the similar results of SRA1 and SRA2 samples after 10 days seems to suggest the existence of a critical SRA dosage. As the reaction progresses, self-desiccation becomes the dominant shrinkage process and the addition of 1.0 and 2.0 wt% SRA could only minimize its effects.

When 3.0 wt% SRA was used, the initial chemical expansion was followed by a period in which self-desiccation imposed a considerable volumetric contraction. The continuous SRA hydration was later able to mitigate such a contraction, with only a slight expansion visible after 10 days.

These results indicate that calcium oxide-rich admixtures can, in fact, be used to control AAM's autogenous shrinkage, but more detailed analysis should be conducted to assess the possible influence of factors such as i) CaO

homogeneous dispersion, b) early age relaxation effects and c) expansion restriction due to a rigid set-up.

### 3.1.2 Drying shrinkage

Drying shrinkage occurs due to the loss of internal water to the external environment through evaporation processes and has been identified as a relevant shrinkage mechanism in alkali-activated materials (Cartwright et al., 2014, Lee et al., 2014). It should be mentioned that the results discussed in this section comprise the contributions of all forms of shrinkage and should be understood as the total shrinkage.

Figure 4a and b show the linear deformation and specific mass variation of  $2 \times 2 \times 16 \text{ cm}^3$  samples up to 56 days. In all samples drying shrinkage was a continuous process, with the highest value recorded in the reference paste after 56 days of curing (21.4 mm/m). As calcium oxide content rose, drying shrinkage was progressively reduced to a minimum of 7.9 mm/m when 3.0 wt% SRA was used (-63%). In all samples, between 76% and 85% of the total drying shrinkage was observed within the initial seven days of curing and a high degree of dimensional stability was reached after 28 days. Mass loss varied from 3% to 4% and occurred mainly in the initial seven days of curing. Total shrinkage has shown a direct correlation with specific mass variation. The reference samples presented the highest shrinkage and mass loss while increasing the SRA dosage progressively reduced the magnitude of those values.

In alkali-activated systems, calcium compounds can possibly contribute to the formation of calcium hydrate species and/or increase the formation of polymeric Si-rich materials. If the former occurs, expanded reaction products are formed and the free water available in the polymeric structures reduces. If the latter, calcium compounds contribute to an increase in the formation of polymeric gel and more stable structures are obtained, thus enhancing their volumetric stability. The microstructural changes imposed by SRA addition along with its effect on pore size distribution will be discussed in the following sections.

Given that surface area may considerably interfere with evaporation processes and consequently affect drying shrinkage, probes of selected samples with different superficial area per unit of volume ratios (h) were produced and

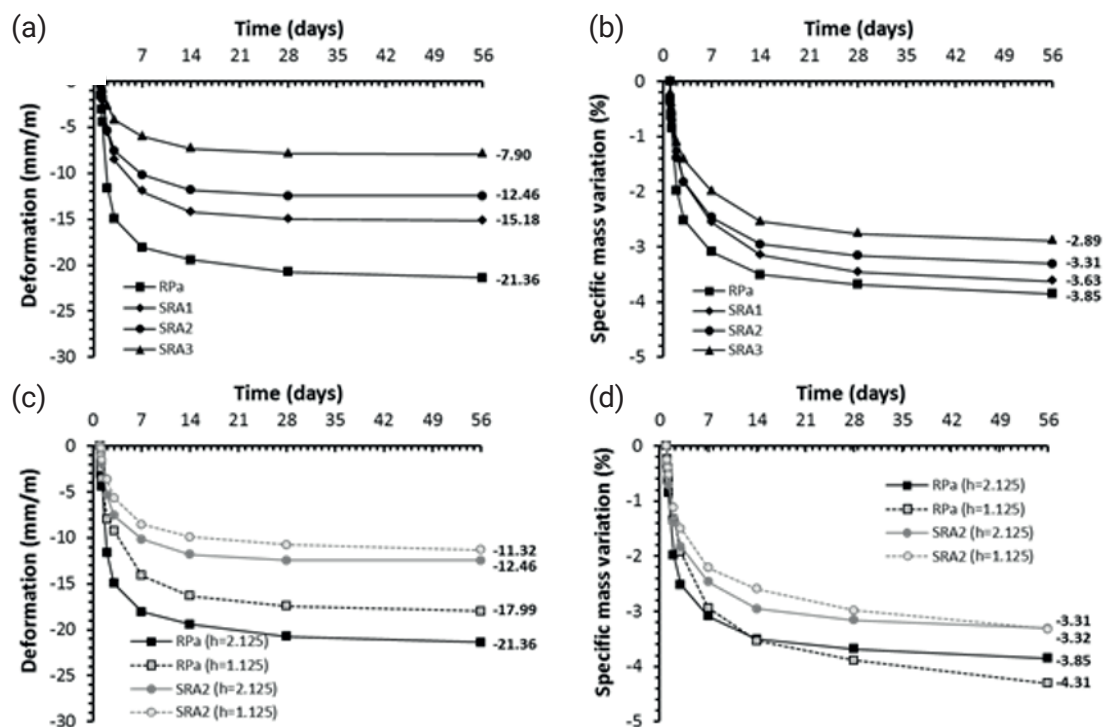


FIGURE 4: Linear deformation (a,c) and specific mass variation (b,d) as function of time, SRA content and surface-to-volume ratio (h).

monitored over 56 days. The results show that by reducing  $h$ , linear deformation decreases, but the magnitude of such reduction mainly depends on SRA presence (see Figure 4c and d). In the reference samples, final linear deformation was decreased by 16% while its specific mass variation increased by 12%. On SRA2 samples, reducing  $h$  resulted in comparable specific mass variations after 56 days, but linear deformation diminished by 9%. In both cases, a more progressive mass loss was promoted, which contributes to a decrease in capillary stress at early ages and an increase in the polymeric structures' volumetric stability.

Therefore, independently of the geometry of the samples produced, commercially available CaO-rich admixtures were found to be an effective SRA that can be used to control AAMs shrinkage. Combined with the previous analysis on setting time and mechanical features (Ascensão et al., 2019b), an optimal admixture dosage of 2.0 wt% is recommended. At this dosage, autogenous and linear drying shrinkage were reduced by 20% and 42%, respectively, while a reasonable fluidity and setting time was maintained to guarantee samples were cast properly. Curing at slightly elevated temperatures could increase the volumetric stability of AAMs (Mastali et al., 2018) and if combined with CaO-rich admixtures led to minimal shrinkage values. However, it is also known that slightly elevated temperature modifies the reaction kinetics and products formed which would have intermingled the effects of these two shrinkage mitigation strategies. Moreover, from the environmental and economic point of view, curing AAMs at room temperature is always preferable. In the context of industrial production, avoid energy-intensive processes that require the implementation of dedicated infrastructures represents significant savings that can dictate the sustainability and

economic viability of alkali-activated products. In addition, curing regimes that require slightly elevated temperatures limit the fields of application of the developed shrinkage mitigation strategies. While such curing conditions can be replicated in some applications (e.g. pre-cast) in other common construction practices such may be challenging (e.g. ready-mix concrete).

## 3.2 Reaction products

### 3.2.1 XRD analysis

Figure 5a and Figure 5b shows a comparison between precursors and AAM patterns, in which it is evident that the produced binders retain a mainly amorphous structure. No significant shift of the broad hump center towards higher  $2\theta$  values was observed. A sharp peak was visible in all patterns, revealing calcite ( $\text{CaCO}_3$ ; PDF 00-005-0586) as the prevalent crystalline phase formed. At later ages, and with increasing SRA content, vaterite ( $\text{CaCO}_3$ ; PDF 01-074-1867), a metastable phase of calcium carbonate, was identified (Figure 5b-d) but the pronounced broad hump and the low magnitude of vaterite's secondary peaks make it hard to postulate its presence. The almost exclusive formation of calcite may indicate silica concentrations near saturation levels and low  $\text{Ca}^{2+}$  to  $\text{CO}_3^{2-}$  activity ratios as the work of Lakshantov et al. (2009) shows that polymeric silica serves as nucleation sites for calcite and inhibits vaterite formation. Moreover, the formation of calcium carbonate species in AAMs has been associated with the high pH of the pore solutions that facilitates the reaction of calcium species with atmospheric  $\text{CO}_2$  (Salman et al., 2105). Along with the presence of calcium species and highly alkaline pore solutions, AAM microstructure also has a determinant effect on the formation of calcium carbonates as it con-

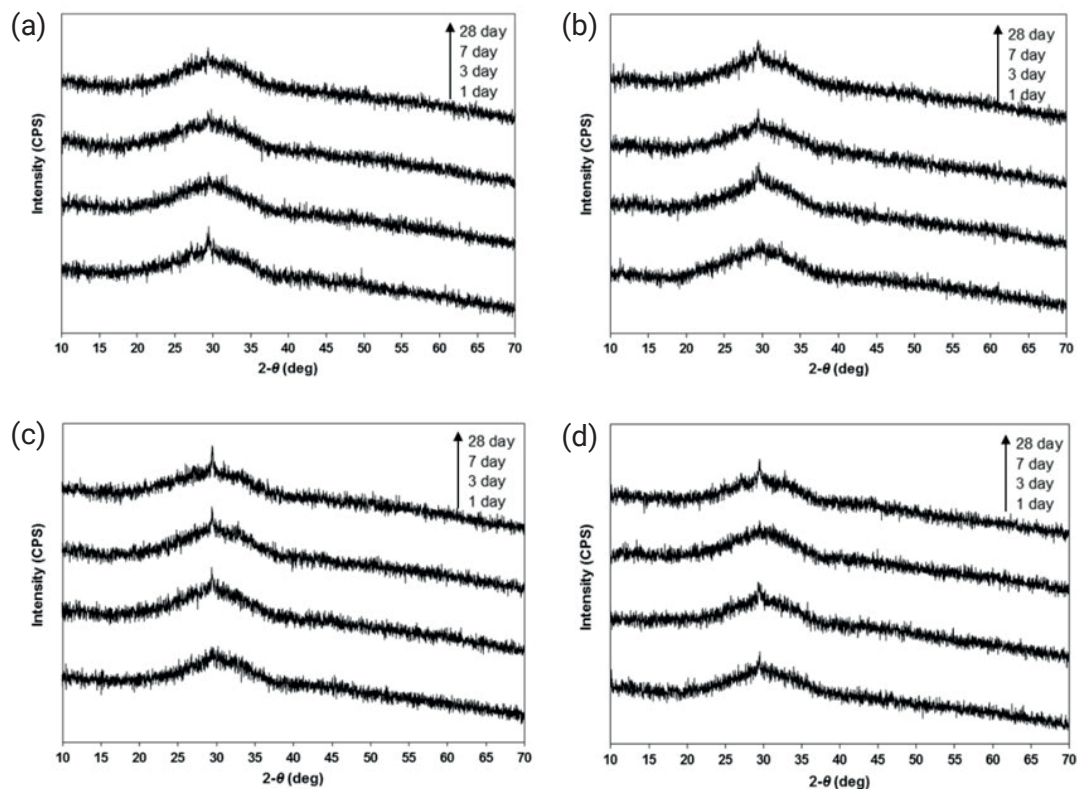


**FIGURE 5:** XRD patterns of AAM samples and their temporal evolution as a function of shrinkage reducing agent content: a) reference paste; b) 1.0 wt% SRA; c) 2.0 wt% SRA and d) 3.0 wt% SRA.

trols the access of atmospheric  $\text{CO}_2$  to the pore solution and inner reaction products.

Thus, although the addition of SRA increases the availability of calcium species, an increase in calcium carbonates was not observed, as XRD patterns show (Figure 5). In fact, the increasing availability of calcium compounds leads to the formation of denser structures when SRA content does not exceed 2.0 wt% (detailed in the “Microstructure” and “Porosity” sections), which restricts atmospheric  $\text{CO}_2$  diffusion and so limits the advance of carbonation. However, this does not apply to the SRA3 samples, where an increase in calcium oxide availability is followed by a slight increase of porosity (Figure 6a), even though carbonation levels remain roughly the same. One explanation may lay in the fact that SRA3 samples present a considerably different pore size distribution (Figure 6b) comprising considerably larger pores that diminish pore-specific surface area and contact area with atmospheric  $\text{CO}_2$ .

Nonetheless, the formation of calcite, which was verified in all samples, can contribute to densification by filling the porous structures and thus enhancing samples’ volumetric stability and mechanical properties as previously reported (Ascensão et al., 2019b).

### 3.3 Microstructure

Figure 7 shows representative backscattered electron imaging micrographs of samples produced with distinct amounts of SRA. A binder phase was formed in all samples, but the existence of unreacted particles confirms that complete dissolution was not achieved (Figure 7a). The

high solid-to-liquid ratio used (3.20) may have limited precursors’ dissolution, but all samples show a homogeneous matrix in which undissolved particles acted as small-sized aggregates (Figure 7a-f). These results are in agreement with previous findings (Machiels et al., 2014), which reported samples with similar S/L ratios as having a degree of precursor’s dissolution of 76 wt%. Although the quantification of unreacted particles has not been performed, a slight decrease in the number of unreacted particles seems to be promoted as SRA content rises.

Depending on solutions’ saturation level with respect to amorphous silica, calcium carbonates, can urge the polymerization of silica in their vicinity (Kellermeier et al., 2010), thus accelerating AAMs’ polymerization. On the other hand, the formation of Ca-precipitates decreases the activating solution pH due to the removal of  $\text{OH}^-$  ions, limiting the precursors’ dissolution and reduces the medium’s supersaturation level. As the authors previously reported (Ascensão et al., 2019b), increasing SRA content led to shorter setting times, which, combined with the reduction of unreacted particles, suggests that the former is favored when small amounts of calcium oxide are added to an already Ca-rich system.

EDS analysis was performed on selected unreacted particles revealing a homogeneous composition constituted by the chemical elements of the main solid precursor, PS (not shown here for the sake of brevity). Some metallic artifacts were detected (as individuated in Figure 7b), which were mainly composed of  $\text{FeO}_x > 90.0$  wt%.

The binder phase of the reference sample has shown

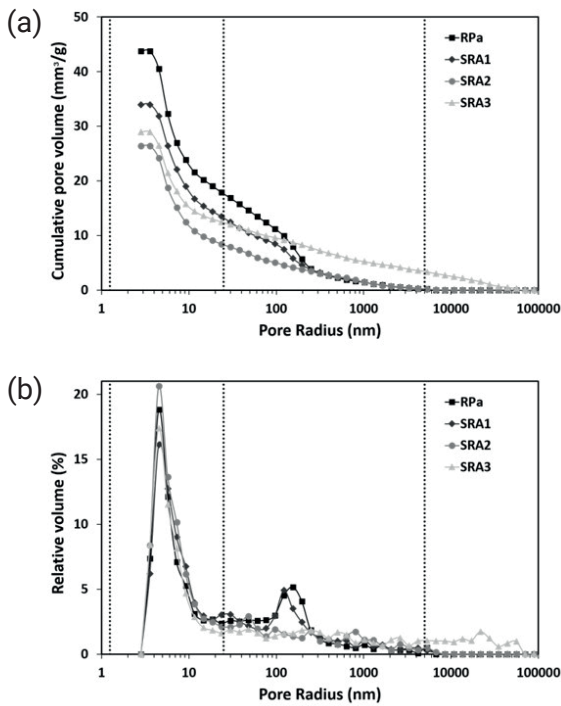


**FIGURE 6:** Cumulative pore volume (a) and relative pore size distribution (b) of samples after 28 days of curing.

to be composed of approximately  $\text{SiO}_2$ :  $\text{CaO}$ :  $\text{Fe}_2\text{O}_3$ :  $\text{Al}_2\text{O}_3$ :  $\text{K}_2\text{O}$  = 2:1:1:0.5:0.2, with the exception of some particular circular areas where an increased content of Si elements was observed (e.g., circular areas identified in Figure 7b).

The higher Si content in these areas may suggest that silica fume particle dissolution occurs at these locations and, due to mobility restrictions imposed by the high viscosity and short open time of the pastes, local heterogeneities were formed in the gel phase (Figure 7b-e). These small circular areas were detected in all samples, however, with a growing Ca content as SRA rose. Furthermore, SRA-containing samples exhibited areas where a Ca-rich gel phase predominated. Figure 7f shows one of those areas in which the binder phase is mainly constituted by a Ca-rich gel (approx.  $\text{SiO}_2$ :  $\text{CaO}$ :  $\text{Fe}_2\text{O}_3$ :  $\text{Al}_2\text{O}_3$ :  $\text{K}_2\text{O}$  = 1:2:0.1:0.2:0.03). In all samples, cracks pierced the binder phase as the undissolved particles limited their propagation. Crack formation and development was particularly severe in Ca-rich binder phases, of which Figure 7f is a representative example. Yet, Ca-rich areas represent a small portion of the binder phase; the cracks formed on those areas are being compensated by the formation of denser and less fractured structures on a macroscopic level. As can be seen in Figure 7b-e, as SRA content increases up to 2.0 wt%, fewer and finer cracks were formed, while with higher SRA dosages more cracks were induced. These results are corroborated by MIP data (detailed in the "Porosity" section), which revealed higher and broader porosity in SRA3 samples. Further, some spherical pores were observed, especially in the reference and SRA1 sample, which can be attributed to air trapped during mixing. Those pores nearly vanished in SRA2 and SRA3 samples, further contributing to the production of dense and me-

chanically strong polymeric structures as shown previously (Ascensão et al., 2019b).

### 3.4 Porosity

Pores can be grouped into four main categories according to size: i) micropores, <1.25 nm; ii) mesopores ranging from 1.25-25 nm; iii) macropores ranging from 25-5000 nm; and iv) entrained and entrapped air voids and pre-existing microcracks >50000 nm (Collins et al., 2000). Micropores are inherent to reaction products whereas capillary pores (comprising both meso- and macropores) can be seen as the residual unfilled spaces between them. Drying shrinkage will greatly depend upon capillary pore size distribution, as it determines the extension and stresses generated by water loss during curing.

Figure 6 presents the cumulative and relative pore size distribution of AAM samples as a function of SRA content. Micropores were outside of the range of measurement and therefore their relative volume is considered negligible. In all samples, the majority of the pores have a pore radius <25 nm and a higher volume of mesopores is concentrated around 5 nm. The amount of mesopores (vol%) increased as calcium oxide dosage rose, from 59 vol% in RPa sample to 68.0 vol% in sample SRA2, and decreased to 57 vol% in sample SRA3. SRA3 samples' hastened viscosity and setting may have compromised their proper confinement and particle packing, increasing the number of voids and cracks in these samples. In fact, Figure 6b shows that SRA3 samples were the only ones containing a proportion of pores with dimensions higher than 10000 nm. These results are in good agreement with the increased amount of visible cracks present in these samples relative to SRA2 (Figure 7b-e) and with the reduction of strength development previously reported (Ascensão et al., 2019b).

## 4. CONCLUSIONS

The use of a calcium oxide-rich admixture to increase the dimensional stability of  $\text{CaO-FeO}_x\text{-Al}_2\text{O}_3\text{-SiO}_2$ -rich alkali-activated materials and its effect on porosity, autogenous and drying shrinkage, mineralogy, and microstructure were studied in this research. The main findings are summarised as follows:

- Drying shrinkage was identified as the governing mechanism affecting AAM volumetric stability, whereas autogenous shrinkage was less significant.
- Calcium oxide-rich admixtures can be effectively used to increase AAMs dimensional stability.
- Shrinkage reduction was proportional to SRA content, but elevated dosages of the latter have a detrimental effect on AAMs microstructure.
- The SRA addition did not induce significant mineralogical changes.

These results demonstrated that commercially available CaO-rich admixtures can be effectively used to control autogenous and drying shrinkage of AAMs. Considering the impacts of CaO-rich admixtures on the remaining AAM properties, a dosage of 2.0 wt% is suggested by the authors.

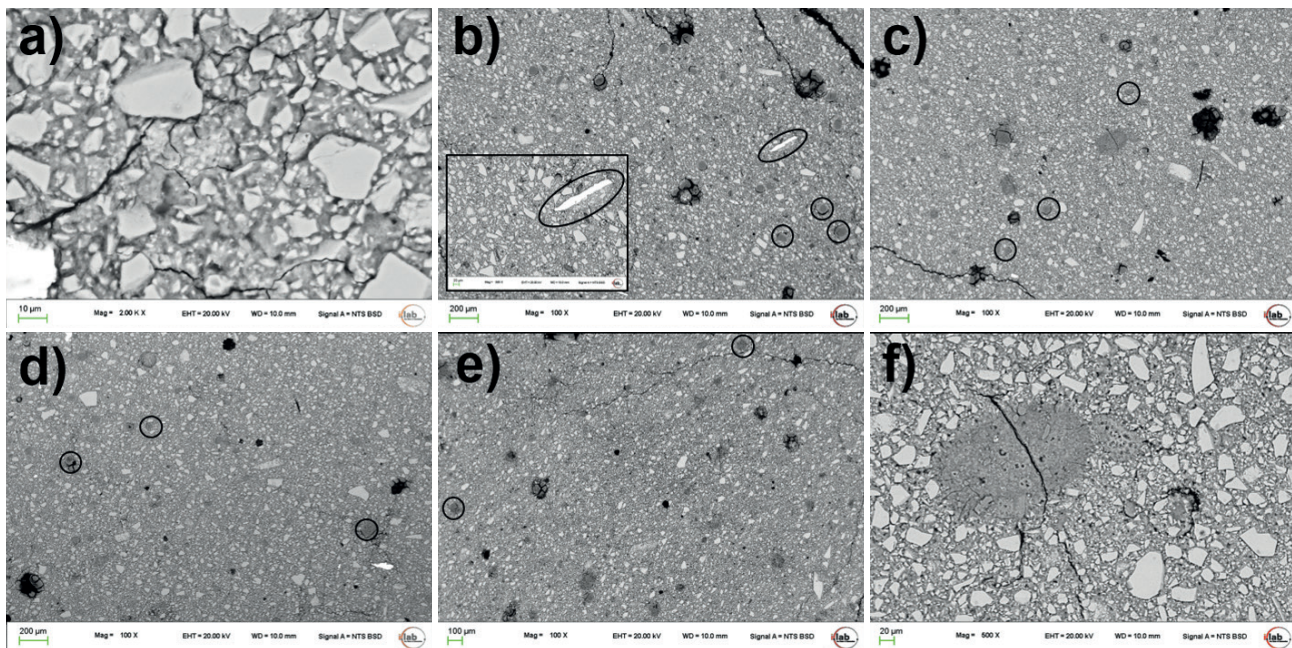


**FIGURE 7:** Backscattered electron imaging micrographs of samples' microstructure and close-ups of selected areas after curing for 28 days: a) reference binder phase and unreacted particles; b) reference paste microstructure; c) 1.0 wt% SRA; d) 2.0 wt% SRA; e) 3.0 wt% SRA and f) Ca-rich binder phase. The insert circles in 7 b-e) show Si-rich binder phases.

Apart from the significant shrinkage reductions obtained, the reduced cost and simple addition method make the use of CaO-rich RSA a promising shrinkage mitigation strategy to increase the performance and competitiveness AAMs relative to benchmark materials.

## ACKNOWLEDGMENTS

This project has received funding from the European Union's EU Framework Programme for Research and Innovation Horizon 2020 under Grant Agreement No 721185. This publication reflects only the author's view, exempting the Community from any liability. Project website: <https://new-mine.ue>.

The authors would also like to thank Mr. Jorn Van de Sande for his invaluable comments, inspirational discussions, and advice.

## REFERENCES

Ascensão, G., Seabra, M. P., Aguiar, J. B., & Labrincha, J. A. (2017). Red mud-based geopolymers with tailored alkali diffusion properties and pH buffering ability. *Journal of Cleaner Production*, 148, 23-30. <https://doi.org/10.1016/j.jclepro.2017.01.150>

Ascensão, G., Marchi, M., Segata, M., Faleschini, F., & Pontikes, Y. (2019a). Reaction kinetics and structural analysis of alkali activated Fe-Si-Ca rich materials. *Journal of Cleaner Production*, 119065. <https://doi.org/10.1016/j.jclepro.2019.119065>

Ascensão, G., Faleschini, F., Marchi, M., Segata, M., & Y Pontikes, Y. (2019b). The effect of calcium-rich admixture on controlling drying shrinkage of alkali activated materials. In *Proceedings of the 6<sup>th</sup> International Slag Valorisation Symposium* (pp. 403-406).

British Standards Institution, BS EN 12617-4:2002 Products and systems for the protection and repair of concrete structures. Test methods, Determination of Shrinkage and Expansion, Milton Keynes, UK, 2002, p. 14

Cartwright, C., Rajabipour, F., & Radlińska, A. (2014). Shrinkage characteristics of alkali-activated slag cements. *Journal of materials in civil engineering*, 27(7), B4014007. [https://doi.org/10.1061/\(ASCE\)MT.1943-5533.0001058](https://doi.org/10.1061/(ASCE)MT.1943-5533.0001058)

Chanvillard, G., Boivin, S., Thierry, J., Guimbal, F., Garcia, D. (2007). U.S. Patent No. 20090305019A1. Washington, DC: U.S. Patent and Trademark Office.

Chen, W., & Brouwers, H. J. H. (2012). Hydration of mineral shrinkage-compensating admixture for concrete: An experimental and numerical study. *Construction and building materials*, 26(1), 670-676. <https://doi.org/10.1016/j.conbuildmat.2011.06.070>

Collins, F., & Sanjayan, J. G. (2000). Effect of pore size distribution on drying shrinking of alkali-activated slag concrete. *Cement and Concrete Research*, 30(9), 1401-1406. [https://doi.org/10.1016/S0008-8846\(00\)00327-6](https://doi.org/10.1016/S0008-8846(00)00327-6)

Corinaldesi, V., Donnini, J., & Nardinocchi, A. (2015). The influence of calcium oxide addition on properties of fiber reinforced cement-based composites. *Journal of Building Engineering*, 4, 14-20. <https://doi.org/10.1016/j.jobee.2015.07.009>

Daux, V., Guy, C., Advocat, T., Crovisier, J. L., & Stille, P. (1997). Kinetic aspects of basaltic glass dissolution at 90 C: role of aqueous silicon and aluminium. *Chemical Geology*, 142(1-2), 109-126. [https://doi.org/10.1016/S0009-2541\(97\)00079-X](https://doi.org/10.1016/S0009-2541(97)00079-X)

Duxson, P., Fernández-Jiménez, A., Provis, J. L., Lukey, G. C., Palomo, A., & van Deventer, J. S. (2007). Geopolymer technology: the current state of the art. *Journal of materials science*, 42(9), 2917-2933. <https://doi.org/10.1007/s10853-006-0637-z>

Gomes, K. C., Lima, G. S., Torres, S. M., de Barros, S. R., Vasconcelos, I. F., & Barbosa, N. P. (2010). Iron distribution in geopolymer with ferromagnetic rich precursor. In *Materials Science Forum* (Vol. 643, pp. 131-138). Trans Tech Publications. <https://doi.org/10.4028/www.scientific.net/MSF.643.131>

Guo, X., & Shi, H. (2015). Metakaolin-, fly ash-and calcium hydroxide-based geopolymers: effects of calcium on performance. *Advances in Cement Research*, 27(10), 559-566. <https://doi.org/10.1680/jadcr.14.00081>

ISO 9277:2010 -Determination of the specific surface area of solids by gas adsorption - BET method.

Jensen, O. M., & Hansen, P. F. (2001). Autogenous deformation and RH-change in perspective. *Cement and Concrete Research*, 31(12), 1859-1865. [https://doi.org/10.1016/S0008-8846\(01\)00501-4](https://doi.org/10.1016/S0008-8846(01)00501-4)

Kellermeier, M., Melero-Garcia, E., Glaab, F., Klein, R., Drechsler, M., Rachel, R., ... & Kunz, W. (2010). Stabilization of amorphous calcium carbonate in inorganic silica-rich environments. *Journal of the American Chemical Society*, 132(50), 17859-17866. <https://doi.org/10.1021/ja106959p>

- Komnitsas, K., Bartzas, G., Karmali, V., Petrakis, E., Kurylak, W., Pietek, G., & Kanasiewicz, J. (2019). Assessment of Alkali Activation Potential of a Polish Ferronickel Slag. *Sustainability*, 11(7), 1863. <https://doi.org/10.3390/su11071863>
- Lakshitanov, L. Z., & Stipp, S. L. S. (2009). Silica influence on calcium carbonate precipitation. *Geochimica et Cosmochimica Acta Supplement*, 73, A716. 2009GeCAS..73Q.716L
- Lee, N. K., Jang, J. G., & Lee, H. K. (2014). Shrinkage characteristics of alkali-activated fly ash/slag paste and mortar at early ages. *Cement and Concrete Composites*, 53, 239-248. <https://doi.org/10.1016/j.cemconcomp.2014.07.007>
- Machiels, L., Arnout, L., Jones, P. T., Blanpain, B., & Pontikes, Y. (2014). Inorganic polymer cement from Fe-silicate glasses: varying the activating solution to glass ratio. *Waste and Biomass Valorization*, 5(3), 411-428. <https://doi.org/10.1007/s12649-014-9296-5>
- Machiels, L., Arnout, L., Yan, P., Jones, P. T., Blanpain, B., & Pontikes, Y. (2017). Transforming enhanced landfill mining derived gasification/vitrification glass into low-carbon inorganic polymer binders and building products. *Journal of Sustainable Metallurgy*, 3(2), 405-415. <https://doi.org/10.1007/s40831-016-0105-1>
- Mastali, M., Kinnunen, P., Dalvand, A., Firouz, R. M., & Illikainen, M. (2018). Drying shrinkage in alkali-activated binders—a critical review. *Construction and Building Materials*, 190, 533-550. <https://doi.org/10.1016/j.conbuildmat.2018.09.125>
- Mounanga, P., Bouasker, M., Pertue, A., Perronet, A., & Khelidj, A. (2011). Early-age autogenous cracking of cementitious matrices: physico-chemical analysis and micro/macro investigations. *Materials and structures*, 44(4), 749-772. <https://doi.org/10.1617/s11527-010-9663-z>
- Neto, A. A. M., Cincotto, M. A., & Repette, W. (2008). Drying and autogenous shrinkage of pastes and mortars with activated slag cement. *Cement and Concrete Research*, 38(4), 565-574. <https://doi.org/10.1016/j.cemconres.2007.11.002>
- Ono, Y., Taketsume, Y., Ogura, H., Takizawa, T. (1997). U.S. Patent No. 3801339A. Washington, DC: U.S. Patent and Trademark Office.
- Pacheco-Torgal, F., Labrincha, J., Leonelli, C., Palomo, A., & Chindaprasit, P. (Eds.). (2014). *Handbook of alkali-activated cements, mortars and concretes*. Elsevier.
- Onisei, S., Lesage, K., Blanpain, B., & Pontikes, Y. (2015). Early age microstructural transformations of an inorganic polymer made of fayalite slag. *Journal of the American Ceramic Society*, 98(7), 2269-2277. <https://doi.org/10.1111/jace.13548>
- Peys, A., White, C. E., Rahier, H., Blanpain, B., & Pontikes, Y. (2019). Alkali-activation of CaO-FeOx-SiO2 slag: Formation mechanism from in-situ X-ray total scattering. *Cement and Concrete Research*, 122, 179-188. <https://doi.org/10.1016/j.cemconres.2019.04.019>
- Provis, J. L. (2014). Geopolymers and other alkali activated materials: why, how, and what?. *Materials and Structures*, 47(1-2), 11-25. <https://doi.org/10.1617/s11527-013-0211-5>
- Sakulich, A. R., & Bentz, D. P. (2013). Mitigation of autogenous shrinkage in alkali activated slag mortars by internal curing. *Materials and structures*, 46(8), 1355-1367. <https://doi.org/10.1617/s11527-012-9978-z>
- Salman, M., Cizer, Ö., Pontikes, Y., Snellings, R., Vandewalle, L., Blanpain, B., & Van Balen, K. (2015). Cementitious binders from activated stainless steel refining slag and the effect of alkali solutions. *Journal of hazardous materials*, 286, 211-219. <https://doi.org/10.1016/j.jhazmat.2014.12.046>
- Simon, S., Gluth, G. J., Peys, A., Onisei, S., Banerjee, D., & Pontikes, Y. (2018). The fate of iron during the alkali-activation of synthetic (CaO-) FeOx-SiO2 slags: An Fe K-edge XANES study. *Journal of the American Ceramic Society*, 101(5), 2107-2118. <https://doi.org/10.1111/jace.15354>
- Thomas, R. J., Lezama, D., & Peethamparan, S. (2017). On drying shrinkage in alkali-activated concrete: Improving dimensional stability by aging or heat-curing. *Cement and Concrete Research*, 91, 13-23. <https://doi.org/10.1016/j.cemconres.2016.10.003>
- Van Deventer, J. S. J., Provis, J. L., Duxson, P., & Lukey, G. C. (2007). Reaction mechanisms in the geopolymeric conversion of inorganic waste to useful products. *Journal of Hazardous Materials*, 139(3), 506-513. <https://doi.org/10.1016/j.jhazmat.2006.02.044>
- Velandia, D. F., Lynsdale, C. J., Provis, J. L., Ramirez, F., & Gomez, A. C. (2016). Evaluation of activated high volume fly ash systems using Na2SO4, lime and quicklime in mortars with high loss on ignition fly ashes. *Construction and Building Materials*, 128, 248-255. <https://doi.org/10.1016/j.conbuildmat.2016.10.076>
- Yang, L., Shi, C., & Wu, Z. (2019). Mitigation techniques for autogenous shrinkage of ultra-high-performance concrete—A review. *Composites Part B: Engineering*, 107456. <https://doi.org/10.1016/j.compositesb.2019.107456>